Electron Acceptor Materials Engineering in Colloidal Quantum Dot Solar Cells

*Huan Liu, Jiang Tang, Illan J. Kramer, Ratan Debnath, Ghada I. Koleilat, Xihua Wang, Armin Fisher, Rui Li, Lukasz Brzozowski, Larissa Levina, and Edward H. Sargent**

Colloidal quantum dot (CQD) photovoltaics combine low-cost solution processibility with precise control over bandgap through the quantum size effect, enabling efficient harvesting of the broad solar spectrum.[1–3] While CQD photovoltaics employing the elegantly simple Schottky configuration have achieved an impressive power conversion efficiency (PCE) of 4.0%,[4] these devices generally suffer from low open-circuit voltage (V_{oc}) and low fill factor (*FF*).[5]

A new architecture, depleted heterojunction CQD (DH-CQD) photovoltaics, was recently reported. This architecture produced the highest-reported CQD device solar power conversion efficiencies of 5.1%.[6]

In CQD sensitized solar cells (QDSSCs), the higher conduction band of CQDs serves as the driving force for electron injection from isolated CQDs to the conduction band and/or defect states of titanium dioxide (TiO_2) electrode.[7,8] The larger the conduction band offset, the better the photogenerated electron injection.[9] DH-CQD photovoltaics follow the same principle. In an array of close packed CQDs, the coupling between delocalized states among adjacent CQDs leads to the establishment of some collective, long-range behaviour characteristics of solids.[10,11] similar to the case in polycrystalline films. The schematic band diagram of a n-type TiO_2 electrode that serves as the electron acceptor for p-type lead sulfide (PbS) CQD DH-CQD device is shown in **Figure 1**a. Fermi level equilibrium between the p-type CQD film and the n-type TiO_2 electrode[6,12–14] leads to the formation of a depletion region on either side of the junction. We represent this as a cascade of quantum-confined levels in the CQD layer, which is similar to band bending in continuous bulk semiconductors. As in the related QDSSC, a favourable conduction band offset further aids in transferring photogenerated electrons from CQD film to the TiO_2 electron acceptor electrode. Majority holes are swept towards the quasi-neutral region and collected by the back ohmic contact. A cross-sectional scanning electron microscopy (SEM) image of the complete DH-CQD device is shown in Figure 1b.

Benefits of the DH-CQD device include

1) placement of the charge-separating interface close to the illumination;
2) hole-blocking at the heterojunction. The optimal band alignment between the PbS CQDs and the TiO_2 is crucial to achieve high device performance.[7]

Ideally, the electron affinity difference should favour electron injection into the TiO_2 without imposing an undue loss of open-circuit voltage. The small binding affinity of excitons in PbS CQDs[15] suggests that only a small–but certainly favourable–offset ($\Delta\chi$) is needed at this junction. Within devices, a favourable band offset will enhance the short-circuit current density (J_{sc}), but once it is sufficiently large, further increase in $\Delta\chi$ will have no further benefits, and will degrade V_{oc}. A device having the optimal power conversion efficiency will manage carefully this delicate balance to maximize the $V_{oc} \times J_{sc} \times FF$ product.

The preceding account describes device operation in a picture of defined bandedges and clean bandgaps. In reality, amorphous and polycrystalline materials, and all imperfectly-passivated interfaces, will exhibit trap state densities. Both shallow and deep traps may impede carrier mobility by producing energetic wells along the transport path. Deep traps can serve as recombination centers for electrons and holes and significantly deteriorate photovoltaic performance.[16] Clearly, a strategy that achieves maximal passivation of each band within the absorber, and of the conduction band within the electron acceptor, is desired.

In light of these requirements–bandedge tunability and passivation–we sought an electrode materials system possessing a number of degrees of freedom that would enable such optimizations. The sol-gel method provides a convenient method of solution deposition and enables the fabrication of continuous, pinhole-free films. It is versatile, allowing incorporation of a wide variety of potential dopants having a uniform distribution.[17,18]

We note that another widely-practiced path to TiO_2 surface optimization relies on functionalization using organic molecules such as phosphonic acids. In dye-sensitized solar cells, this approach successfully tunes the band position of TiO_2 electrodes.[19] We found that, in our devices, this strategy generally failed to improve device performance. We propose that the highly concentrated treatments applied repeatedly to our colloidal quantum dot layers

Dr. H. Liu,[+] Dr. J. Tang,[+] I. J. Kramer, Dr. R. Debnath,
G. I. Koleilat, Dr. X. H. Wang, Dr. A. Fisher,
Dr. R. Li, Dr. L. Brzozowski, Dr. L. Levina, Prof. E. H. Sargent
Department of Electrical and Computer Engineering
University of Toronto
10 King's College Rd., Toronto
Ontario M5S 3G4, Canada
E-mail: ted.sargent@utoronto.ca
Dr. H. Liu
Department of Electronic Science and Technology
Huazhong University of Science and Technology
1037 Luoyu Rd., Wuhan
Hubei 430074, China
[+] H.L. and J.T. contributed equally to this work.

DOI: 10.1002/adma.201101783

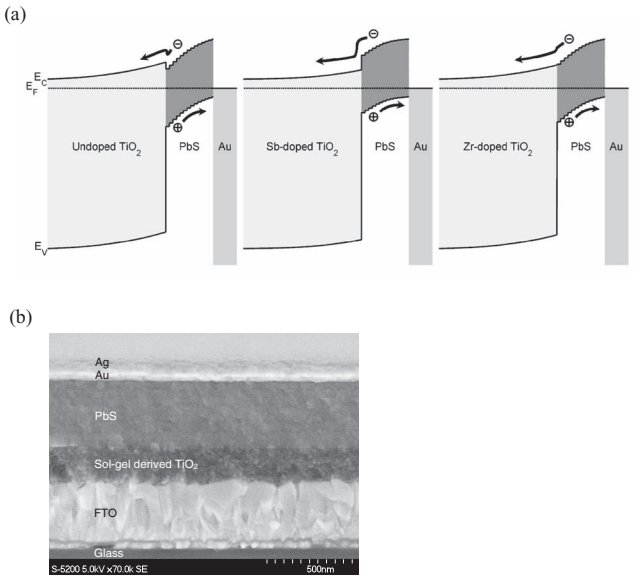

Figure 1. (a) Schematic band diagram of the DH-CQD devices at equilibrium. The right panel shows the optimal band alignment that combines maximal charge separation with high open-circuit voltage. (b) Cross-sectional SEM image of the device. The thickness of sol-gel derived TiO_2 layer is ~200 nm.

residing atop the electrode may have overwhelmed the impact of the initial electrode-modifying treatments.

In a quest to find a TiO_2 electrode that paired optimally with our PbS CQD layers, we set out to explore the material and electronic properties of sol-gel derived TiO_2 electrodes. We first found conditions that produced crack-free TiO_2 electrodes (see the Experimental Section). We then systematically investigated the incorporation of various metal ions to tune the properties of TiO_2. We explored Mg, Sb, In, Al, Bi, Zr, Si, V, Pb, and Nb doping. We found that Zr, Al, Sb, and Nb showed promising improvements in CQD photovoltaic performance compared to undoped TiO_2. Zr and Al-doped TiO_2 electrodes behaved similarly to one other; and Sb and Nb to one another. We thus selected three materials–undoped, Sb-doped and Zr-doped TiO_2–for detailed investigation herein.

Fourier transform infrared spectroscopy (FTIR) study showed no appreciable C-H vibration in the film, indicating complete removal of organic components by the heat treatment (Figure S1a). X-ray diffraction (XRD) investigation indicated that undoped, Sb-doped and Zr-doped TiO_2 were all well crystallized into the anatase phase, (101) being the strongest diffraction peak with no appearance of the main peak (110) of the rutile phase (Figure S1b). Optical transmission spectra showed that all these electrodes had nearly identical transmission in the spectral region from 300–800 nm (Figure S1c). In addition, the optical bandgaps of the undoped, Sb-doped and Zr-doped TiO_2 were estimated to lie in the narrow range 3.26–3.29 eV using the Tauc plot of $[\alpha(h\nu)]^{1/2}$ versuss. $h\nu$ (Figure S1d). Such values are the same as for pristine TiO_2 without band narrowing.[20] X-ray photoelectron spectroscopy (XPS) revealed that the Ti 2p and O 1s peaks were indistinguishable for the differently-doped TiO_2 electrodes. In all cases, Ti^{4+} was the only type of Ti cations. The Sb and Zr dopants were identified as Sb^{5+} and Zr^{4+} species respectively (Figure S2 and Table S1).

Next we sought to quantify electron mobility and free carrier density in each TiO_2 using field effect transistor (FET) measurements.[21,22] The FET device structure and the drain current-gate voltage (I_d–V_g) characteristics are shown in **Figure 2**a. As expected, we observed n-type modulation with small gate leakage (Figure S3). From the measured transconductance (Figure S4), we obtained a linear mobility of electrons in the range 0.01–0.03 $cm^2\ V^{-1}\ s^{-1}$ for each TiO_2. Doping did not–within the accuracy of our mobility measurement technique–alter electron mobility.

Knowing mobility and conductance allowed us to estimate the free carrier density in each TiO_2. **Table 1** summarizes the material properties of each sol-gel derived TiO_2. The undoped

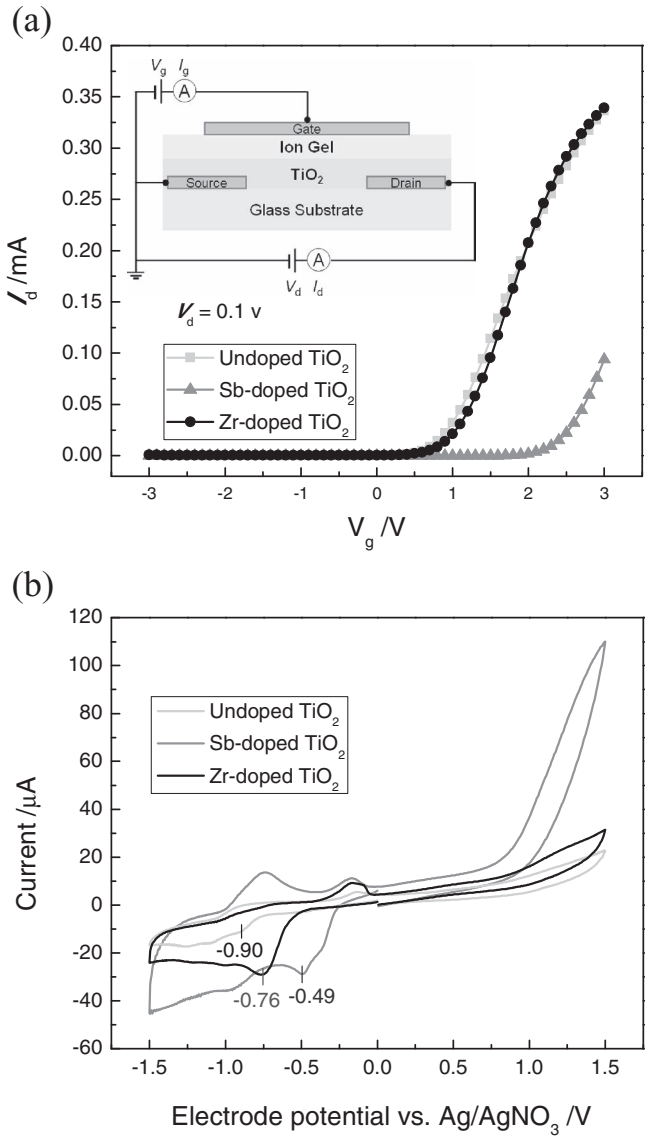

Figure 2. (a) Transfer characteristics (I_d vs. V_g) in the linear regime (V_d = 0.1 V) of the ion-gel top-gated FET with different TiO_2 to deduce the electron mobility and threshold voltage. The inset depicts the ion-gel top gated FET device structure. The TFT has a channel length of 2.5 μm and channel width of 2.0 mm. (b) Cyclic-voltammetry scans of TiO_2 electrodes in a solution of $TBAPF_6$ in anhydrous acetonitrile.

Table 1. Summary of the material properties of different sol-gel derived TiO_2.

TiO_2	Crystalline structure	Optical bandgap [`eV]	Conduction bandedge [eV]	Electron mobility [$cm^2 V^{-1} s^{-1}$]	Threshold voltage [V]	Vertical conductivity [$S\ cm^{-1}$]	Carrier density [cm^{-3}]
Undoped TiO_2	Anatase	3.28	–3.81	0.015	0.9	5.3 E-6	2.2 E15
Sb-doped TiO_2	Anatase	3.26	–4.22	0.015	2.4	3.1 E-5	1.3 E16
Zr-doped TiO_2	Anatase	3.29	–3.95	0.026	1.1	1.4 E-5	3.4 E15

and Zr-doped TiO_2 showed similar free carrier densities in the low 10^{15} cm^{-3} range, while the Sb-doped was in the low 10^{16} cm^{-3}. The threshold voltage (V_{Th}) was consistent with this carrier density trend: it was in the vicinity of ~1 V for undoped and Zr-doped, and a much larger 2.4 V for the Sb-doped TiO_2 channel FET.

In summary, neither of the dopants significantly changed carrier transport, and only Sb led to a notable increase in free carrier density under our preparation conditions. In all cases, the electrodes were lightly-doped n-type materials having the same bandgap as unmodified anatase TiO_2.

Of crucial interest was knowledge of the positions of TiO_2 conduction bandedges. For this we employed cyclic-voltammetry (C-V) method where the reduction potential provides information on the location of the conduction bandedge (CB) and the electronic state distribution.[23,24] In Figure 2b, the potential of Ag/$AgNO_3$ reference electrode was calibrated as –4.71 V,[25] therefore the undoped TiO_2 was the shallowest with CB at –3.81 eV; the Zr-doped electrode somewhat deeper at –3.95 eV; and the Sb-doped TiO_2 deepest at –4.22 eV. In addition, the C–V scans revealed dramatic differences in current amplitude near the onset of the conduction bandedge. Whereas undoped TiO_2 was much weaker, both doped TiO_2 electrodes have much higher amplitudes similar to one another. The chemical capacitance monitored by C–V scans is proportional to the density of states,[26,27] We thereby successfully increased the density availability of states near the conduction bandedge of TiO_2 by Sb or Zr doping.

We fabricated photovoltaic devices using each TiO_2 electrode. A 400 nm-thick PbS CQD film was fabricated via layer-by-layer quantum dot deposition followed by treatment of each layer using 3-mercaptopropionic acid in methanol (see the Supporting Information). Current density vs. voltage characteristics under AM1.5 illumination are shown in **Figure 3**a. The control devices (using undoped sol-gel TiO_2) showed a J_{sc} of 11.3 mA cm^{-2} and a PCE of 3.66%, similar to the reported PbS CQD devices also employing sol-gel derived TiO_2.[28] Compared to the control devices, solar cells based on Sb or Zr-doped TiO_2 electrodes showed much improved PCE arising primarily from a 50% increase in J_{sc}.

The enhanced electron injection into doped TiO_2 is confirmed by the external quantum efficiency spectra (EQE) acquired under 1 sun solar light bias shown in Figure 3b. Zr-doped TiO_2 devices based on the same PbS CQD film, the only difference being the choice of electrode, showed higher EQE across the entire absorbing region compared to undoped TiO_2. This finding suggests that it is the transfer of photogenerated carriers across the interface–rather than any change in depletion or collection within the absorbing quantum dot film–that led to enhanced carrier separation.

Since the hysteresis originating from diode capacitance has the potential to lead to the overestimation of photovoltaic device efficiency inferred from a current-voltage scan,[29,30] we took special care to monitor any hysteresis in current-voltage scanning in our PCE measurements. As seen in the Supporting Information (Figure S5), fast scan (0.1 V/s) produced an ~6% overestimation of PCE. Therefore, we developed a testing protocol that would eliminate the effects of any hysteresis on efficiency estimates and ensure steady-state power conversion efficiencies are

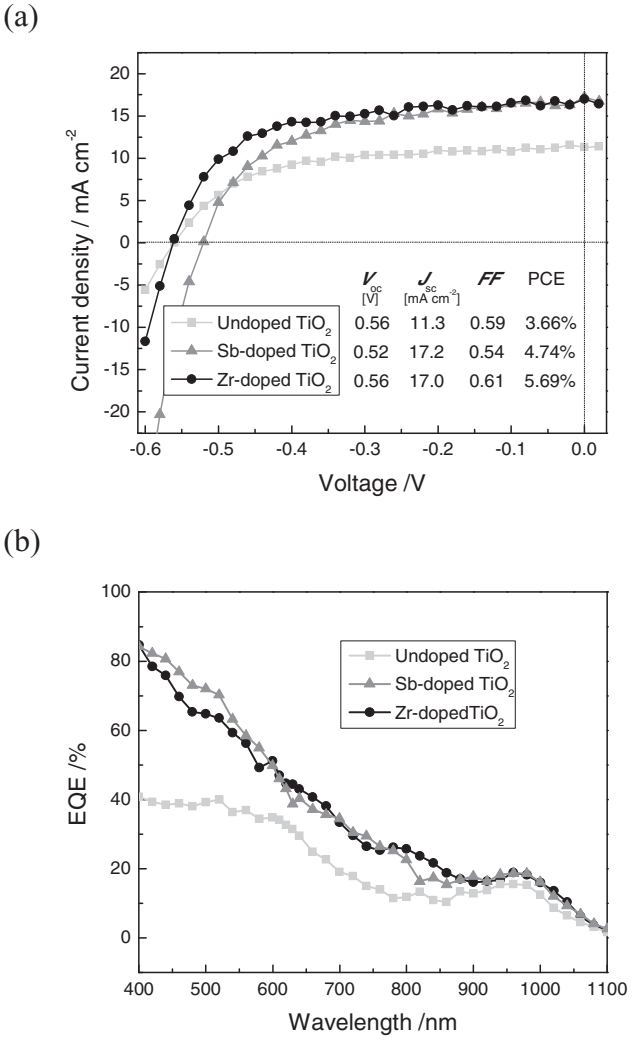

Figure 3. (a) Current density-voltage characteristics of devices with different TiO_2 electrodes under simulated solar light. (b) 1 sun solar light-biased EQE spectra of the devices.

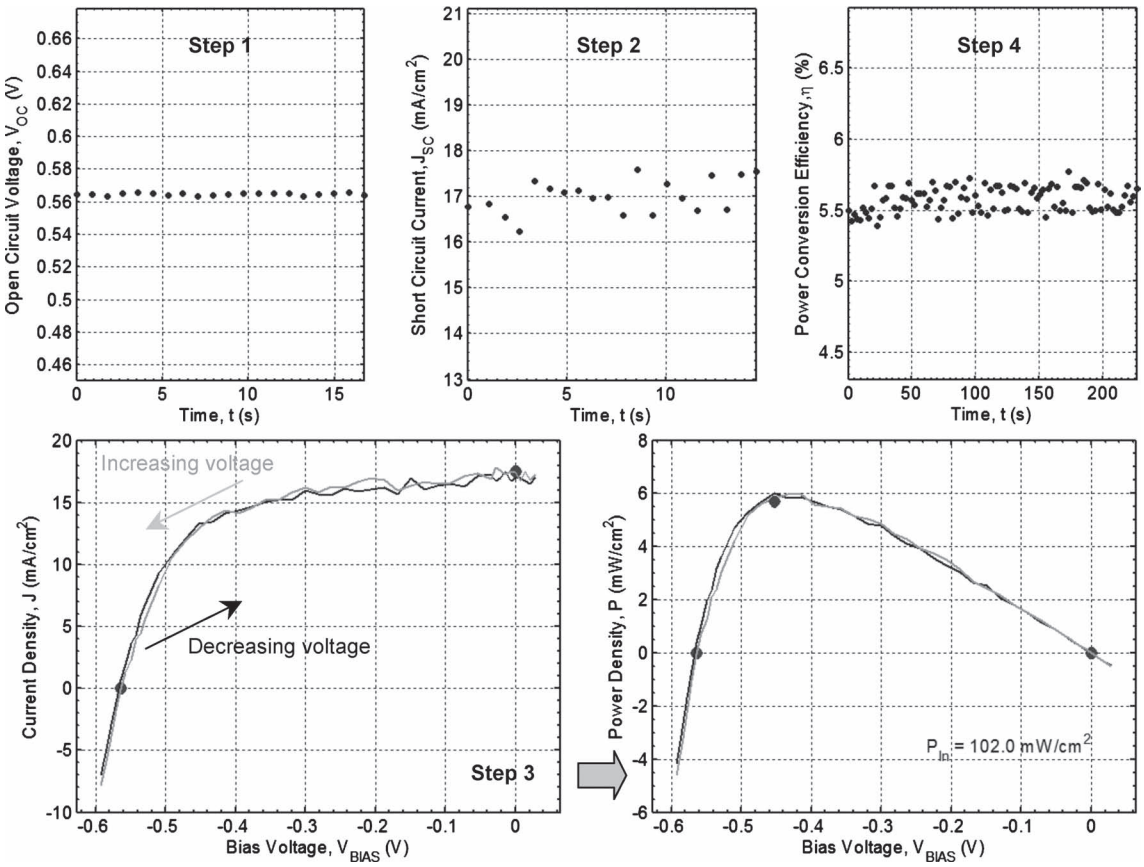

Figure 4. Performance of the champion PbS/Zr-doped TiO_2 device measured at static mode. Voc was first obtained (Step 1) at zero output current; and J_{sc} then measured (Step 2) at zero output voltage. The current density was then measured as the voltage was swept in a decreasing and increasing direction successively (Step 3). Corresponding output power density was calculated and depicted in the right Step 3 panel. The device was then operated at the maximum power point to monitor its static power conversion efficiency (Step 4).

reported (see the Experimental Section). All efficiencies reported herein rely on monitoring the electrical power transferred by the solar cell to an optimal load (chosen to achieve the maximum power point, MPP) for several minutes. Using Zr-doped TiO_2 electrode, we have fabricated more than 20 devices with efficiency >5.2%: V_{oc} of 0.54–0.60 V and J_{sc} of 15–18 mA cm^{-2}. The champion device in **Figure 4** had a V_{oc} of 0.56 V, J_{sc} of 17.0 mA cm^{-2}, and a solar power conversion efficiency of 5.6%.

We now discuss the origin of the improved electron injection in the CQD photovoltaics using Sb-doped and Zr-doped TiO_2. We investigated the possibility that the electrodes might exhibit different morphologies leading to larger surface areas or larger areas of contact between the quantum dots and the electrode. Our premise was that these might be the source of improved electron injection. From atomic force microscopy (AFM) we found quite similar surface roughness in the range 2.9–3.3 nm for all TiO_2 electrodes (Figure S6). The possibility of significant differences in carrier transport within each electrode was eliminated by the electron mobility measurements reported above. The EQE study, and also the efficiency trends, argues against the view that the higher free carrier density in the Sb electrode played a major role in enhancing extraction via a deepened depletion region within the absorbing colloidal quantum dot film.

We propose that one primary mechanism explains the effectiveness of the optimal electrodes.

The conduction bandedge lies near –3.90 eV for the 950 nm-wavelength-bandgap PbS CQDs employed herein.[31] Electron injection is most strongly favoured into Sb-doped TiO_2, and remains favourable into Zr-doped. In both cases the increased availability of states near the conduction bandedges contributes to the injection improvement as well. However, an unfavourable band offset serves as injection barrier is present in the undoped case. These band offsets are consistent both with the higher J_{sc} values for Sb- and Zr-doped electrodes, and also with the deteriorated V_{oc} in the Sb-doped case. The Zr-doped TiO_2 electrode manages this delicate balance near-optimally. We believe that the band diagrams shown in the left, middle and right panel of Figure 1a represent the undoped, Sb-doped and Zr-doped case, respectively.

This picture of subtle tuning of band alignment is further confirmed by additional studies in which smaller-bandgap PbS CQDs were employed, producing an ~0.1 eV lowering in the quantum-confined bandedge of the absorbing layer.[15] As seen in **Table 2**, the Sb-doped electrode continues to favour strong injection, but now the Zr-doped loses performance regardless of the increased density of states, and undoped TiO_2 remains inefficient.

Table 2. Representative photovoltaic performance for 1200 nm-wavelength-bandgap PbS CQDs/TiO_2 solar cells (AM1.5 light intensity = 102 mW/cm^2).

PbS CQDs	TiO_2	V_{oc} [V]	J_{sc} [mA cm^{-2}]	*FF*	PCE
1200 nm-wavelength-bandgap	Undoped TiO_2	0.39	10.1	0.45	1.74%
	Sb-doped TiO_2	0.36	19.1	0.46	3.10%
	Zr-doped TiO_2	0.38	12.9	0.46	2.21%

In summary, by doping sol-gel derived TiO_2 with Zr, we have successfully engineered the band structure of the photo-generated electron-accepting TiO_2 electrode to best match the conduction band position of an optimal-single-junction-bandgap colloidal quantum dot film. This resulted in improved charge separation at the PbS/TiO_2 interfaces with no sacrifice to open-circuit voltage. The resultant solar cell yielded a highest-reported CQD device solar power conversion efficiency of 5.6%.

Experimental Section

TiO_2 Electrode Preparation: The sol-gel derived TiO_2 electrodes were fabricated by depositing Ti-sols on FTO substrates (25 mm × 25 mm, Pilkington TEC15) using spin-coating with following heat treatment. The preparation of Ti-sols was carried out in air ambient at room temperature. Titanium (IV) n-butoxide (4.25 mL) was mixed with triethanolamine (3.75 mL) and anhydrous ethyl alcohol (25 mL) in a flask under continuous magnetic for 2 h, where antimony (III) ethoxide (106 µL) or zirconium ethoxide (0.17 g) would be added respectively for Sb- or Zr-doped TiO_2 electrodes, Sb/Ti or Zr/Ti molar ratio both being 5%. Acetic acid (5 mL) and deionized water (5 mL) were then added into the mixture with continuous magnetic agitation for 24 h. The mixture was then stored in a beaker and placed inside fumehood to allow condensation reactions until the volume reached 15 mL. Before spin-coating, the FTO substrates were sonicated in a mixture of Triton in de-ionized water (2% by volume) and then in isopropanol and de-ionized water sequentially. 20 drops of the Ti-sols were deposited on the FTO substrates by spin-coating at 2500 RPM for 15 s. One edge of the as-deposited film was then wiped free of the sols with a swab soaked in anhydrous ethyl alcohol to expose a region of clean FTO for electrical contacting. This wipe was immediately followed by heat treatment in air on a hotplate at 520 °C for 1 hour.

Cyclic-Voltammetry Measurement: We carried out the C-V measurement at room temperature on PalmSens electrochemical station inside a N_2-glovebox, using Ag/$AgNO_3$ (Ag wire within $AgNO_3$ anhydrous acetonitrile solution, 0.01 M) as the reference electrode and Pt wire as the counter electrode. The TiO_2 electrodes served directly as the working electrode and their macroscopic areas in C-V measurement were kept the same to within 10%. Tetrabutylammonium hexaflurophosphate (0.1 M) in anhydrous acetonitrile was used as the supporting electrolyte. The scan rate was 0.1 V/s with direction 0 V → –1.5 V → 0 V → 1.5 V → 0 V. Using the ferrocene/ferricinum redox (–4.80 V relative to vacuum) as the standard reference, we calibrated the potential of Ag/$AgNO_3$ reference electrode as –4.71 V relative to vacuum.

PbS CQD Synthesis and Device Fabrication: PbS CQDs and solar cells were prepared using a variation on a literature method.[6] Gold contacts (15 nm thick) were deposited by thermal evaporation at a rate of 0.4 Å/s, followed by thermal evaporation of silver contacts (90 nm thick) at a rate of 1.0 Å/s with base pressure of 1×10^{-7} mbar. The deposition was carried out in Angstrom Engineering Åmod deposition system in an Innovative Technology glovebox. Contact sizes were 0.061 cm^2.

PCE Measurement: Current density-voltage characteristics were measured using a Keithley 2400 source-meter in N_2 ambient. The solar spectrum at AM1.5 was simulated to within class A specifications (less than 25% spectral mismatch) with a Xe lamp and filters (Solar Light Company Inc.) with measured intensity at 102 mW cm^{-2}. The source intensity was measured with a Melles-Griot broadband power meter and a Thorlabs broadband power meter through a circular 0.049 cm^2 aperture at the position of the device and confirmed with a calibrated reference solar cell (Newport, Inc.). The accuracy of the power measurement was estimated to be ±7%. Four strategies were employed in combination to reduce errors in estimating power conversion efficiency:

1) We calculated the efficiency by dividing the entire power conveyed through the 0.049 cm^2 aperture onto the devices (0.061 cm^2). We also checked the static J_{sc} in larger area devices (0.25 cm^2) and obtained the same values as in the small area devices.
2) We periodically calibrated the spectral mismatch between our simulator spectrum and the reference spectrum ASTM G173-03.
3) To avoid any efficiency overestimation originated from hysteresis, we measured the current density-voltage characteristics using different scan rates and different sweep directions to figure out a hysteresis-free scanning protocol which is in good agreement with the static measurement.
4) The device was then operated at the maximum power point for an extended period to monitor its static power conversion efficiency.

SEM and EQE Characterization: SEM characterization was obtained on Hitachi S-5200 scanning electron microscope. The external quantum efficiency spectrum was acquired under 1 sun solar light bias by passing the output of a 400 W Xe lamp through a monochromator and using appropriate order-sorting filters. The resultant monochromatic beam also passed through an optical chopper operating at a frequency of 100 Hz coupled to the input of a Stanford Research Systems lock-in amplifier. The collimated output of the monochromator was measured through a 0.0079 cm^2 aperture with calibrated Newport 818-UV and Newport 818-IR power meters as needed. The measurement step was 20 nm and the intensity varied with the spectrum of the Xe lamp. The monochromatic light was co-aligned with an AM 1.5 source (Newport Corporation) providing one-sun intensity of continuous white light bias. The photogenerated current was then measured using a lock-in amplifier.

Supporting Information

Supporting Information is available from the Wiley Online Library or from the author.

Acknowledgements

This publication is based in part on work supported by Award No. KUS-11-009-21, made by King Abdullah University of Science and Technology (KAUST), by the Ontario Research Fund Research Excellence Program, and by the Natural Sciences and Engineering Research Council (NSERC) of Canada. The authors thank Angstrom Engineering and Innovative Technology for useful discussions regarding material deposition methods and control of glovebox environment, respectively. We would also like to acknowledge the technical assistance and scientific guidance of E. Palmiano, R. Wolowiec and D. Kopilovic. H. Liu would like to acknowledge the scholarship from China Scholarship Council (CSC). R. Debnath and I. J. Kramer acknowledge the financial support through e8/MITACS Elevate Strategic Fellowship and the Queen Elizabeth II/Ricoh Canada Graduate Scholarship in Science and Technology, respectively.

Received: May 12, 2011
Published online: July 14, 2011

[1] E. H. Sargent, *Nat. Photonics* **2009**, *3*, 325.
[2] A. J. Nozik, M. C. Beard, J. M. Luther, M. Law, R. J. Ellingson, J. C. Johnson, *Chem. Rev.* **2010**, *110*, 6873.
[3] J. Tang, E. H. Sargent, *Adv. Mater.* **2011**, *23*, 12.
[4] K. Szendrei, W. Gomulya, M. Yarema, W. Heiss, M. A. Loi, *Appl. Phys. Lett.* **2010**, *97*, 203501.
[5] J. M. Luther, M. Law, M. C. Beard, Q. Song, M. O. Reese, R. J. Ellingson, A. J. Nozik, *Nano Lett.* **2008**, *8*, 3488.
[6] A. G. Pattantyus-Abraham, I. J. Kramer, A. R. Barkhouse, X. Wang, G. Konstantatos, R. Debnath, L. Levina, I. Raabe, M. K. Nazeeruddin, M. Gratzel, E. H. Sargent, *ACS Nano* **2010**, *4*, 3374.
[7] I. Mora-Sero, J. Bisquert, *J. Phys. Chem. Lett.* **2010**, *1*, 3046.
[8] A. Braga, S. Gimenez, I. Concina, A. Vomiero, I. Mora-Sero, *J. Phys. Chem. Lett.* **2011**, *2*, 454.
[9] D. F. Wang, H. G. Zhao, N. Q. Wu, M. A. El Khakani, D. L. Ma, *J. Phys. Chem. Lett.* **2010**, *1*, 1030.
[10] H. W. Hillhouse, M. C. Beard, *Curr. Opin. Colloid Interface Sci.* **2009**, *14*, 245.
[11] C. W. Jiang, M. A. Green, *J. Appl. Phys.* **2006**, *99*, 114903.
[12] J. M. Luther, J. B. Gao, M. T. Lloyd, O. E. Semonin, M. C. Beard, A. J. Nozik, *Adv. Mater.* **2010**, *22*, 3704.
[13] K. W. Johnston, A. G. Pattantyus-Abraham, J. P. Clifford, S. H. Myrskog, S. Hoogland, H. Shukla, J. D. Klem, L. Levina, E. H. Sargent, *Appl. Phys. Lett.* **2008**, *92*, 122111.
[14] J. B. Gao, J. M. Luther, O. E. Semonin, R. J. Ellingson, A. J. Nozik, M. C. Beard, *Nano Lett.* **2011**, *11*, 1002.
[15] F. W. Wise, *Acc. Chem. Res.* **2000**, *33*, 773.
[16] S. A. Ringel, A. W. Smith, M. H. Macdougal, A. Rohatgi, *J. Appl. Phys.* **1991**, *70*, 881.
[17] M. Gratzel, *J. Sol-Gel Sci. Tech.* **2001**, *22*, 7.
[18] U. G. Akpan, B. H. Hameed, *Appl. Catal. A-Gen.* **2010**, *375*, 1.
[19] P. Wang, S. M. Zakeeruddin, P. Comte, R. Charvet, R. Humphry-Baker, M. Gratzel, *J. Phys. Chem. B* **2003**, *107*, 14336.
[20] X. B. Chen, S. S. Mao, *Chem. Rev.* **2007**, *107*, 2891.
[21] M. S. Kang, J. Lee, D. J. Norris, C. D. Frisbie, *Nano Lett.* **2009**, *9*, 3848.
[22] M. S. Kang, A. Sahu, D. J. Norris, C. D. Frisbie, *Nano Lett.* **2010**, *10*, 3727.
[23] E. Kucur, W. Bucking, T. Nann, *Microchim. Acta* **2008**, *160*, 299.
[24] J. Bisquert, F. Fabregat-Santiago, I. Mora-Sero, G. Garcia-Belmonte, E. M. Barea, E. Palomares, *Inorg. Chim. Acta* **2008**, *361*, 684.
[25] H. Z. Zhong, S. S. Lo, T. Mirkovic, Y. C. Li, Y. Q. Ding, Y. F. Li, G. D. Scholes, *ACS Nano* **2010**, *4*, 5253.
[26] V. G. Kytin, J. Bisquert, I. Abayev, A. Zaban, *Phys. Rev. B* **2004**, *70*, 193304.
[27] J. Garcia-Canadas, F. Fabregat-Santiago, H. J. Bolink, E. Palomares, G. Garcia-Belmonte, J. Bisquert, *Synth. Met.* **2006**, *156*, 944.
[28] T. Ju, R. L. Graham, G. M. Zhai, Y. W. Rodriguez, A. J. Breeze, L. Yang, G. B. Alers, S. A. Carter, *Appl. Phys. Lett.* **2010**, *97*, 043106.
[29] J. M. Gordon, E. A. Katz, W. Tassew, D. Feuermann, *Appl. Phys. Lett.* **2005**, *86*, 073508.
[30] W. Guter, A. W. Bett, *IEEE Trans. Electron Dev.* **2006**, *53*, 2216.
[31] B. R. Hyun, Y. W. Zhong, A. C. Bartnik, L. F. Sun, H. D. Abruna, F. W. Wise, J. D. Goodreau, J. R. Matthews, T. M. Leslie, N. F. Borrelli, *ACS Nano* **2008**, *2*, 2206.